Nanoscale

PAPER

Check for updates

Exploiting cyanine dye J-aggregates/monomer equilibrium in hydrophobic protein pockets for efficient multi-step phototherapy: an innovative concept for smart nanotheranostics†

Matías L. Picchio, [a] Julian Bergueiro, [b,c] Stefanie Wedepohl, [b] Roque J. Minari, [d] Cecilia I. Alvarez Igarzabal, [a] Luis M. Gugliotta, [d] Julio C. Cuggino *[d] and Marcelo Calderón *[e,f]

After several decades of development in the field of near-infrared (NIR) dyes for photothermal therapy (PTT), indocyanine green (ICG) still remains the only FDA-approved NIR contrast agent. However, upon NIR light irradiation ICG can react with molecular oxygen to form reactive oxygen species and degrade the ICG core, losing the convenient dye properties. In this work, we introduce a new approach for expanding the application of ICG in nanotheranostics, which relies on the confinement of self-organized J-type aggregates in hydrophobic protein domains acting as monomer depots. Upon the fast photobleaching, while the dye is irradiated, this strategy permits the equilibrium-driven monomer replacement after each irradiation cycle that radically increases the systems' effectivity and applicability. Gadolinium-doped casein micelles were designed to prove this novel concept at the same time as endowing the nanosystems with further magnetic resonance imaging (MRI) ability for dual-modal imaging-guided PTT. By teaching a new trick to a very old dog, the clinical prospect of ICG will undoubtedly be boosted laying the foundation for novel therapeutics. It is anticipated that future research could be expanded to other relevant J-aggregates-forming cyanine dyes or nanocrystal formulations of poorly water-soluble photosensitizers.

1. Introduction

Photothermal therapy (PTT) is one of the most efficient non-invasive therapies that can induce cellular death of malignant tumors with minimal side effects compared with traditional chemotherapy or radiotherapy.[1,2] With the emergence of the innovative concept of oncolytic nanoreactors, PTT has gained renewed attention in the last three years, as it can be synergistically combined in cascade reactions with other therapeutic modalities as starvation, oxygenation and/or chemodynamic therapies.[3–6]

Near-infrared (NIR) irradiation with wavelengths in the range of 700–1100 nm, are usually used in PTT to achieve high tissue penetration because living tissues display negligible absorbance and autofluorescence in this NIR region.[7] Among the many NIR photothermal agents available, noble-metal-based nanostructures,[8,9] carbon nanomaterials,[10–12] and semiconductor[13,14] nanoparticles have been extensively studied in cancer therapy. However, clinical translation of this type of nanomaterials has been limited due to their non-degradable nature that jeopardizes long-term biosafety.[15] For this reason, organic dyes are usually preferred as contrast agents for PTT. Although an assortment of organic chromophores has been developed in the last decade, indocyanine green (ICG) is currently the only NIR-absorbing dye approved by the US food and drug administration (FDA).[16] However, the clinical use of ICG has been restricted due to its poor optical

[a]Departamento de Química Orgánica, Facultad de Ciencias Químicas, Universidad Nacional de Córdoba, IPQA, CONICET-UNC, Haya de la Torre y Medina Allende. Ciudad Universitaria, Córdoba, X5000 HUA, Argentina
[b]Freie Universität Berlin, Institut für Chemie und Biochemie, Takustrasse 3, 14195 Berlin, Germany
[c]Centro Singular de Investigación en Química Biolóxica e Materiais Moleculares (CiQUS), Departamento de Química Orgánica, Universidade Santiago de Compostela, Spain
[d]Instituto de Desarrollo Tecnológico para la Industria Química (INTEC), CONICET-UNL, Güemes 3450, Santa Fe 3000, Argentina.
E-mail: jcuggino@intec.unl.edu.ar
[e]POLYMAT, Applied Chemistry Department, Faculty of Chemistry, University of the Basque Country UPV/EHU, Paseo Manuel de Lardizabal 3, 20018 Donostia-San Sebastián, Spain
[f]IKERBASQUE, Basque Foundation for Science, 48009 Bilbao, Spain.
E-mail: marcelo.calderon@polymat.eu
†Electronic supplementary information (ESI) available. See DOI: 10.1039/d0nr09058a

stability, low aqueous solubility, and short blood residence time (half-life of 4 min).[17] To tackle these limitations, extensive effort has been made to encapsulate ICG in various nanoparticle formulations, including liposomes,[18] micelles,[19] and polymeric nanoparticles.[20] These strategies have proven to be effective for addressing the dye pharmacokinetics, but the photothermal degradation of ICG still remains the main challenge that has hampered its widespread use in clinical applications.[21,22]

In 1936, E. Jelley discovered the molecular aggregation phenomenon of pseudo-isocyanine chloride (PIC),[23] introducing the concept of J-aggregates which have a bathochromic shift as a hallmark. Since then, plenty of work has been done concerning the light absorption properties of cyanine dyes. One year later, Scheibe conducted a comprehensive study using different organic cyanines, solvents, dye concentrations, and temperatures, concluding that the bathochromic shift in the J-band absorption spectrum is due to reversible supramolecular self-organization of the dye monomers.[24,25] ICG is a cyanine dye that also undergoes such organization process.

Recently, Dai et al. demonstrated that ICG self-organized into J-type aggregates (J-ICG) exhibits significantly improved photothermal stability as compared with the monomeric dye.[26] These J-aggregates, ranging 5–20 nm in diameter,[27] are featured by a narrow red-shifted absorbance peak at 890 nm, and interestingly, they coexist in equilibrium with monomeric and dimeric dye forms. Unfortunately, these promising assemblies fail in in vivo applications as they are not thermodynamically stable in serum and dissociate within minutes.[28]

Under this scenario, we hypothesized that J-ICG could be confined in a hydrophobic environment and prevent their uncontrolled dissociation. Moreover, the J-aggregate/monomer equilibrium could be exploited to improve the ICG performance in light to heat transduction derived from its poor photostability. Indeed, confined J-ICG could act as a monomer reservoir where photobleached ICG monomer would be quickly replaced by the J-ICG/monomer equilibrium (Scheme 1).

Consequently, multiple NIR-irradiation steps could be efficiently performed with minimal detriment to the heat generation in each cycle.

In order to prove this novel concept, we proposed confining J-ICG into the hydrophobic pockets of a casein micellar structure. The choice of this type of nanocarrier was motivated by two key points. On the one hand, ICG has a high binding affinity for proteins such as serum albumin[29,30] or ferritin.[31] Thus, an effective interaction can also be envisioned for caseins as they have many hydrophobic domains available for dye stabilization. Besides, ICG could ionically interact with cationic and anionic groups from glutamic acid, aspartic acid, and lysine residues of caseins. On the other hand, by designing a protein-based nanocarrier, we intend to address characteristic long-term toxicity issues, the bottleneck for the clinical translation of several promising nanomedicines. Conveniently for biological applications, casein micelles (CM) can be degraded by enzymes like trypsin or cathepsin B, typically overexpressed in tumor microenvironments, ensuring an efficient body clearance after nanocarrier application.[32,33]

Altogether, CM fit the requirements as a J-aggregates stabilization platform but still needs to prove their versatility in multimodal applications. Indeed, CMs stability in biological environments is itself a main concern for nanocarrier design.[34] To address this point, we evaluated the covalent crosslinking of CMs via carbodiimide chemistry using diethylenetriaminepentaacetic acid gadolinium(III) (DTPAGd) as a reticulating agent (Fig. 1). Gadolinium (Gd^{3+})-based contrast agents were widely used for enabling magnetic resonance imaging (MRI) or magnetic resonance angiography (MRA) in nanovehicles.[35,36] For example, Gd^{3+}-decorated polymeric nanomaterials have shown an increased Gd^{3+} tumor accumulation and improved MRI detection.[37–39] Moreover, Gd^{3+} complexes are compatible with photothermal dyes like ICG, enabling their combination for dual-modal imaging and phototherapy-synergized tumor ablation.[40]
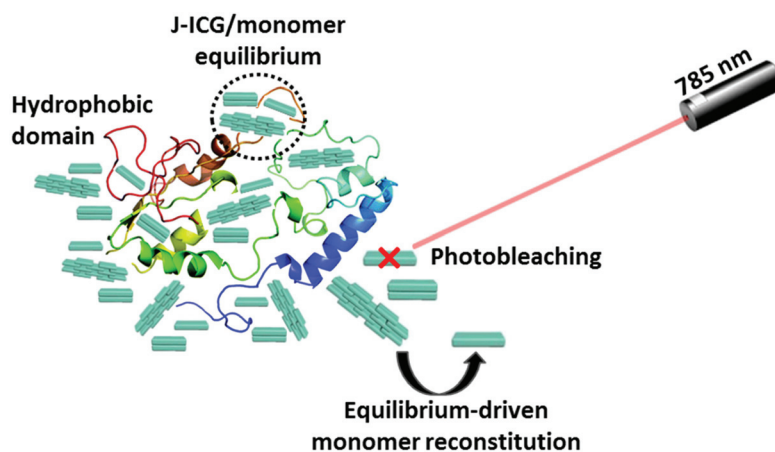
Scheme 1 Illustration of the concept of J-ICG/monomer equilibrium-driven dye reconstitution. J-ICG are stabilized into hydrophobic domains of β-casein, one of the major components of the micelles.
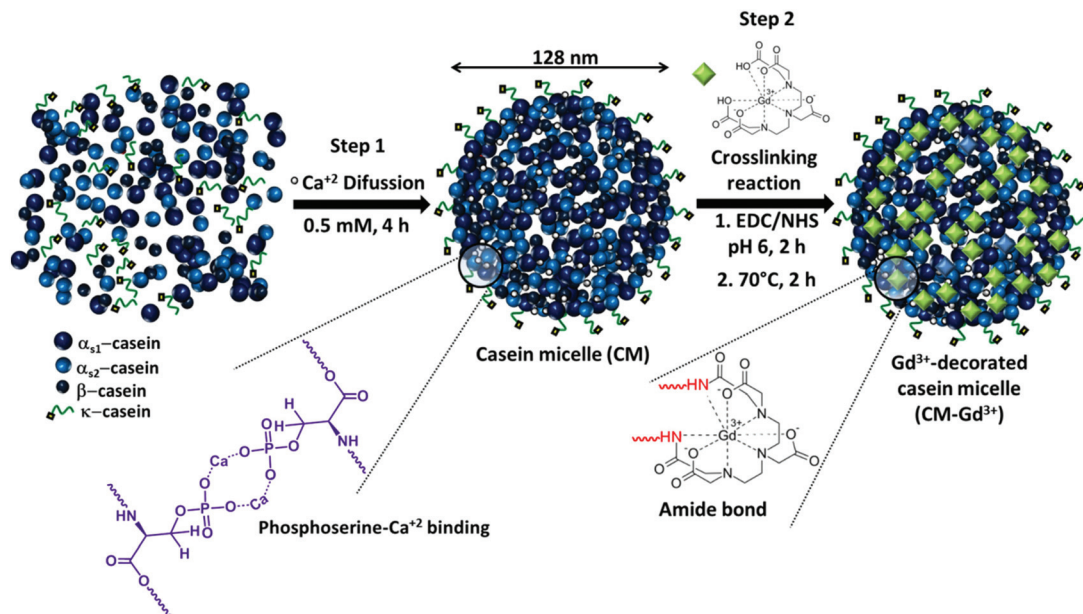
Fig. 1 General procedure for yielding the CM-Gd nanocarriers. Step 1: Re-assembly of CM through calcium ionic interactions. Step 2: Micelles crosslinking by using DTPAGd as a reticulating agent.

In the study presented herein we engineered Gd^{3+}-decorated CMs that can stabilize J-ICG into their hydrophobic pockets acting as a reservoir for equilibrium-driven monomer dye reconstitution. Various micelle formulations were prepared by varying the content of the reticulating agent to control their nanostructure and resistance against cathepsin B as a model protease. *In vitro* studies showed that the extra stabilization offered by this type of biocompatible micelles can guarantee the long-term supply of ICG monomer into cancer cells and achieve a higher efficiency as PTT agent. With dual-modal MRI/NIR-fluorescence imaging (NIRFI) and multi-step PTT capabilities, our platform has the potential to open up new avenues in nanotheranostics.

2. Results and discussion

We followed a two-step procedure for the construction of our protein-based nanocarriers (Fig. 1). In the first step, CM were prepared following a protocol already described by our group elsewhere.[34] This method is based on the re-assemblage of CM using a $CaCl_2$ solution that stabilizes the micelles with ionic interactions between Ca^{2+} and the phosphoserine residues of casein. Stable micelles with sizes in the range of 125–150 nm and with low dispersity and high reproducibility were obtained (see Fig. S1 of the ESI†).

In the second step, DTPAGd was incorporated into CM by using amidation methodology. First, the free acid groups of DTPAGd were activated to *N*-hydroxysuccinimide form and subsequently reacted with the free amino groups of casein. This strategy aimed to confer structural stability to the micelles as an extra crosslinking point and provide the

system with MRI capability. Different amounts of DTPAGd were tested to find the CM decoration possibilities that also ensure that the parental physicochemical properties are maintained. Thus, four amounts of DTPAGd were used to reach Gd^{3+} incorporations of 1.6 (CM-Gd$_2$), 4.4 (CM-Gd$_4$), 6.4 (CM-Gd$_6$), and 7.3 weight % (CM-Gd$_7$) as was confirmed by ICP-MS.

The sizes of the Gd^{3+} decorated CM (CM-Gd$_x$) were measured by dynamic light scattering (DLS) at 37 °C and pH 7.4 and 5 emulating physiological conditions of plasma and endolysosomal compartments, respectively (Fig. 2a). The CM-Gd$_x$ presented *Z*-averages by DLS in the range between 140 and 165 nm at plasma pH and 37 °C. The obtained sizes were confirmed by nanoparticle tracking analysis (NTA) at a lower concentration (thousand times below the casein critical micelle concentration) (see Fig. S2a of the ESI†). These size values were similar to the ones obtained for reassembled CM (128 nm), indicating a negligible inter-micelle crosslinking. A clear hydrodynamic diameter trend at different crosslinking degrees was not observed, having in all cases similar values. This behaviour suggests that ionic assembly in the nanostructuration step turned the micelles into a relatively stable template, limiting volume changes upon further covalent reticulation. Similar results were obtained at an emulated lysosomal pH of 5. But in this case, CM and the least crosslinked nanocarrier (CM-Gd$_2$) were not colloidally stable and underwent aggregation. Such aggregation phenomenon is probably due to the electrostatic destabilization of those less rigid nanostructures, as the isoelectric point of casein is 4.6 and an approximately neutral charge is expected for the micelles at pH 5. These results prove that the covalent stabilization by DTPAGd in the CM-Gd improved their colloidal stability in
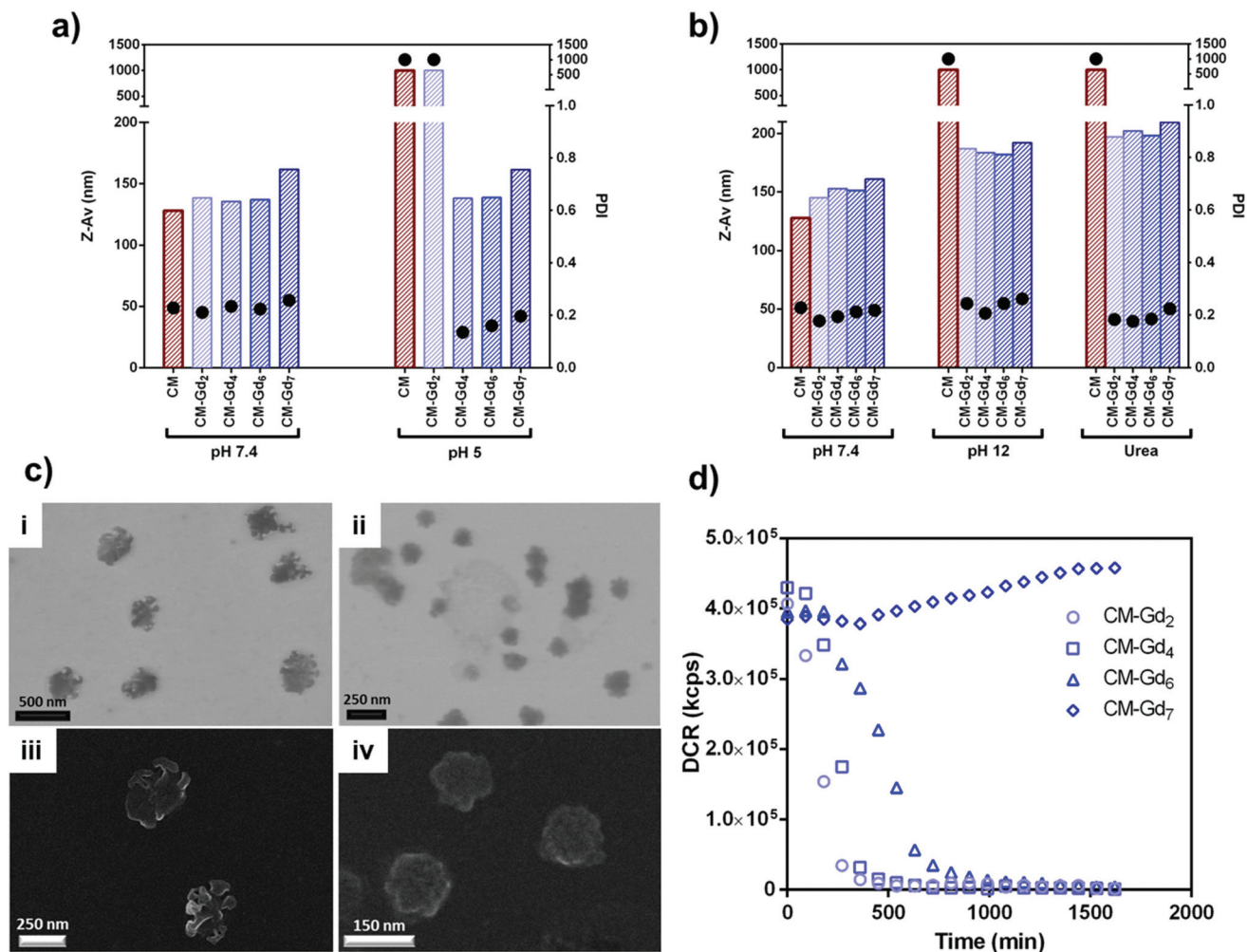
Fig. 2 (a) Hydrodynamic size (bars) and PDI (dots) in emulated physiological conditions. (b) Colloidal stability of CM-Gd$_x$ after addition of urea or strong alkaline medium at 25 °C. (c) Morphologies of CM-Gd$_2$ (i and iii) and CM-Gd$_7$ (ii and iv) determined by STEM at different magnifications. (d) Change of number of particles in dispersion upon proteolytic degradation with cathepsin B, expressed as derived count rate (DCR) measured by DLS.

mild acidic conditions. In this sense, it is desirable that the nanocarrier maintains its structure in the bloodstream long enough to guarantee its accumulation in the tumour target site. Bearing this in mind, further stability studies were performed for CM-Gd$_x$ by following the average size by DLS using urea and strong alkaline pH (pH 12) as destabilizing agents (Fig. 2b). These agents were selected because they can disrupt hydrogen bonding and hydrophobic interactions, and solubilize colloidal calcium, respectively.[41,42] While CM were rapidly dissociated after the addition of urea or at pH 12, all the CM-Gd$_x$ maintained their structural integrity, and only small increases in their average size were observed. This result shows the effectiveness of the covalent crosslinking process which maintains the casein chain of the micelles bound.

In addition, the morphologies of CM-Gd$_2$ and CM-Gd$_7$ were analyzed by scanning transmission electron microscopy (STEM) (Fig. 2c). CM-Gd$_7$ showed a more compact structure than CM-Gd$_2$, probably due to a densely crosslinked network

was obtained for this system, which agrees with the stability behavior discussed above. CM-Gd$_2$ presented a greater diameter (200–220 nm) in a dry state than CM-Gd$_7$ (130–150 nm), according to the crosslinking degree of these nanosystems.

Cancer-associated proteases are commonly overexpressed in the tumour microenvironment, which has been widely used for triggering the release of oncologic drugs in smart modalities.[43] With our nanocarrier design we expect to exploit this proteases overexpression for promoting body clearance after therapy. In this sense, it is desirable that micelles conserve their structural integrity long enough to ensure J-ICG stabilization during the treatment before being degraded. Starting from this premise, we hypothesized that the proteolytic cleavage rate of the micelles could be controlled by the crosslinking density of these nanostructures. To shed some light on this, we studied the degradation behaviour of CM-Gd$_x$ by DLS, using cathepsin B as a model protease at a physiologically relevant concentration. The evol-

ution of the derived count rate (DCR) was followed over time (Fig. 2d), as this parameter is directly related to the number of particles in the dispersion. As it can be seen, DCR decreased early and steadily for the least crosslinked system suggesting a fast disassembly of the micelle structure upon addition of cathepsin B. Similar behaviour was observed for CM-Gd$_4$ and CM-Gd$_6$. Still, in these cases, the onset of the DCR decay, which could be correlated to the beginning of the micelles degradation, occurred slightly later than CM-Gd$_2$, 90 and 180 min, respectively. Interestingly, in contrast with these results, the most crosslinked nanocarrier (CM-Gd$_7$) showed a relatively constant value of DCR over the experiment, suggesting a very slow fragmentation for this system. Additional evidence of this phenomenon was found when analyzing the number-weighted particle size distributions (PSD) of CM-Gd$_7$, which showed a shifting over time to smaller sizes (Fig. S2b of the ESI†). We hypothesized that highly compact nanonetworks might act as a barrier to the enzyme's penetration into the micelles, limiting the protein degradation rate. Altogether, these results demonstrate that by increasing the crosslinking density of the micelles, the rate of proteolytic degradation could be controlled for an effective therapeutic application. Indeed, this robust nanostructure confers superior stability to CM-Gd$_7$ in physiological environments, and thus it

was chosen for proving our concept of J-ICG stabilization and equilibrium-driven monomer supply.

J-ICG in water at room temperature are in equilibrium with their monomeric and dimeric form of the dye and each structure presents a different NIR characteristic absorption maximum of: monomeric (780 nm), dimeric (715 nm), and J-ICGs (895 nm) (Fig. 3a).[26,44] In our strategy, J-ICG confined in CM-Gd$_7$ (CM-Gd$_7$-J-ICG) serves as a reservoir for the long-term supply of ICG monomer. For this, we tested the stabilization properties of CM-Gd$_7$ by using different amounts of encapsulated J-ICG (1, 5, 10, and 15 wt%). In all cases, encapsulation efficiencies (EE) larger than 90% were found (Fig. 3b). The colloidal stability of CM-Gd$_7$-J-ICG, for a dye concentration of 15 wt%, was evaluated by DLS in different media (Fig. S3†). The obtained sizes were 159, 166, and 165 nm in water, buffers pH 7.4, and pH 5, respectively, in good agreement with the size of the unloaded system.

We also evaluated the *in situ* J-aggregation of ICG within the micelles, but interestingly the dye self-assembly was not attained even at high temperature, probably due to strong protein/dye interactions, which hampered the self-organization of the monomer molecules (see Fig. S4 of the ESI† for more details). The stability of J-ICG aggregates encapsulated in CCM-Gd$_7$ was investigated following the evolution over time of
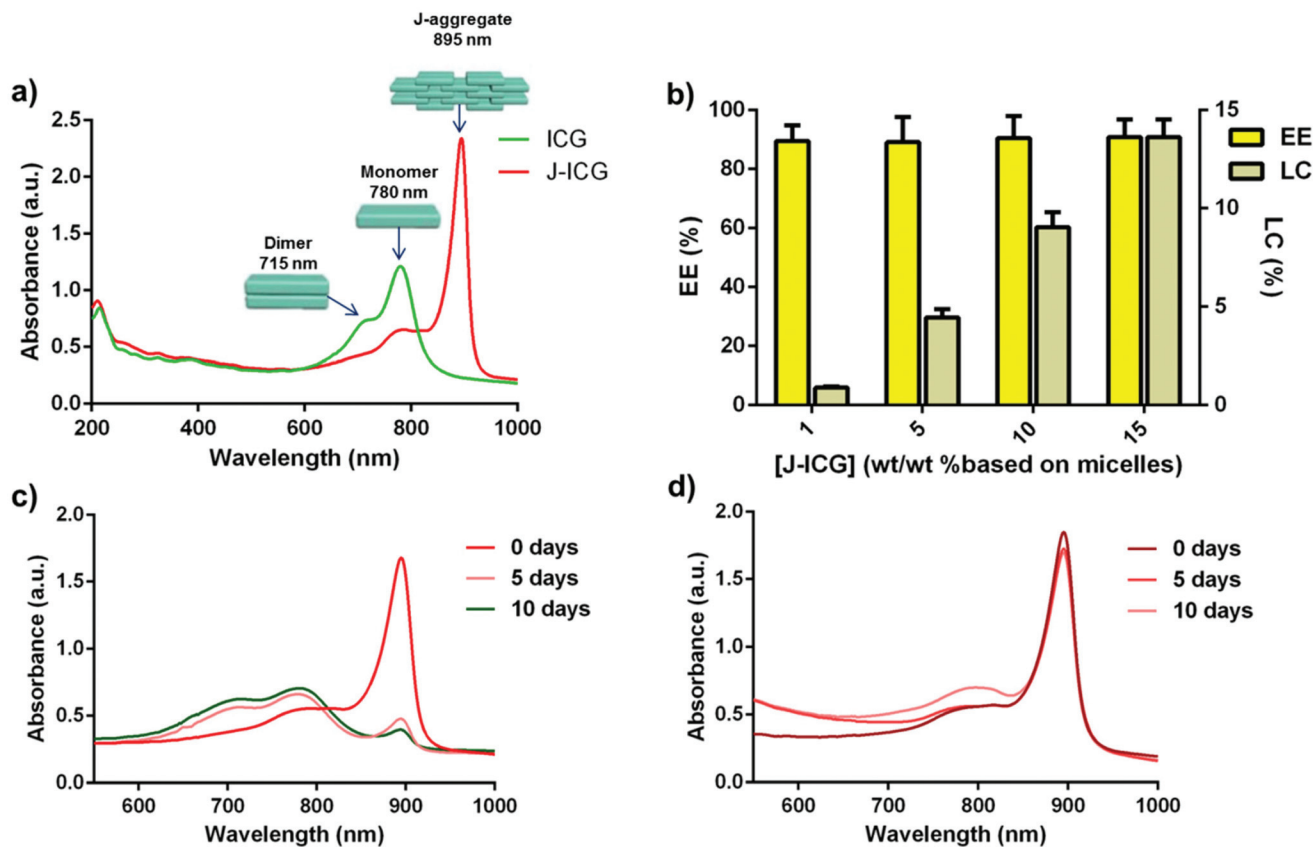

Fig. 3 (a) UV-Vis spectra of ICG and J-ICG showing their characteristic absorption peaks. (b) Encapsulation efficiency (EE) and loading capacity (LC) of J-ICG in CM-Gd$_7$ for different micelles/dye ratios. Evolution over time of UV-Vis spectra of (c) free J-ICG and (d) CM-Gd$_7$-J-ICG.

the characteristic J-ICG trace in the UV-Vis region using non-encapsulated J-ICG as a control. J-ICG was preserved in the interior of the micelles for at least 10 days, doubling the stability of non-encapsulated J-ICG, which was dissociated in 5 days (Fig. 3c and d). These results suggest that the encapsulation of J-ICG in our nanocarrier notably increases its stability long enough to be applied in PTT.

To validate our proposed concept of equilibrium-driven ICG monomer reconstitution, the NIR-light to heat transducing capability of the CM-Gd$_7$-J-ICG was studied by recording the heat generation upon repeated NIR laser (785 nm) irradiation cycles. As expected, ICG in its monomeric form was photobleached upon laser irradiation, with a notable decrease in the maximum temperature reached after each cycle (Fig. 4a). On the contrary, J-ICG as a control showed virtually the same performance in all four irradiation cycles (reaching temperatures as high as 68 °C), supporting the concept of using them as ICG monomer depots. CM-Gd$_7$-J-ICG showed a heat generation superior to free ICG monomer but unexpectedly lower than J-ICG (at a dye concentration of 25 μg mL^{-1}) (Fig. 4a). In order to get insight into this behaviour we studied the change of the NIR characteristic absorption of ICG, J-ICG, and CM-Gd$_7$-J-ICG upon each irradiation cycle. It becomes obvious that the irradiation of the monomer always results in a continuous decrease of their characteristic absorption peaks at 715 and 780 nm upon each cycle (Fig. S5a†). In contrast, when irradiat-

ing J-ICG at 785 nm the ICG photodegradation drove the disassembly of the J-aggregate, showing an important decrease of its characteristic peak at 895 while maintaining the absorbance of the dimeric and monomeric form unchanged (Fig. 4b). In other words, J-ICG acts as depots for the continuous supply of monomer/dimer ICG. Similar behaviour was observed for CM-Gd$_7$-J-ICG, but curiously, confined J-ICG disassembled faster than the free form so that no aggregates were evidenced from the end of the second cycle (Fig. 4c). We speculate that this unexpected behaviour could be related to the generation of local gradients of high temperatures in the confined environment that can accelerate the disassembly rate of the aggregated form, as they can degrade above 80 °C.[44] Nevertheless, the temperature values reached by CM-Gd$_7$-J-ICG after four cycles of irradiation (around 59 °C at the tested concentration) are high enough to provoke cellular ablation.[45] In fact, the photothermal efficiencies of free J-ICG and our nanoplatform calculated from a single ON/OFF cycle were quite similar, 13% and 11%, respectively (see Fig. S5b and eqn (S1)†). Ultimately, we checked the integrity of the protein nanocarriers after multiple photothermal applications (four cycles) by analyzing their PSD by DLS. After irradiations, no significant changes were found in the PSD, supporting the robustness of our nanosystem (data not shown).

In our design, Gd^{3+}-complex was chosen as a functional crosslinker to endow to the system MRI capabilities. This prop-
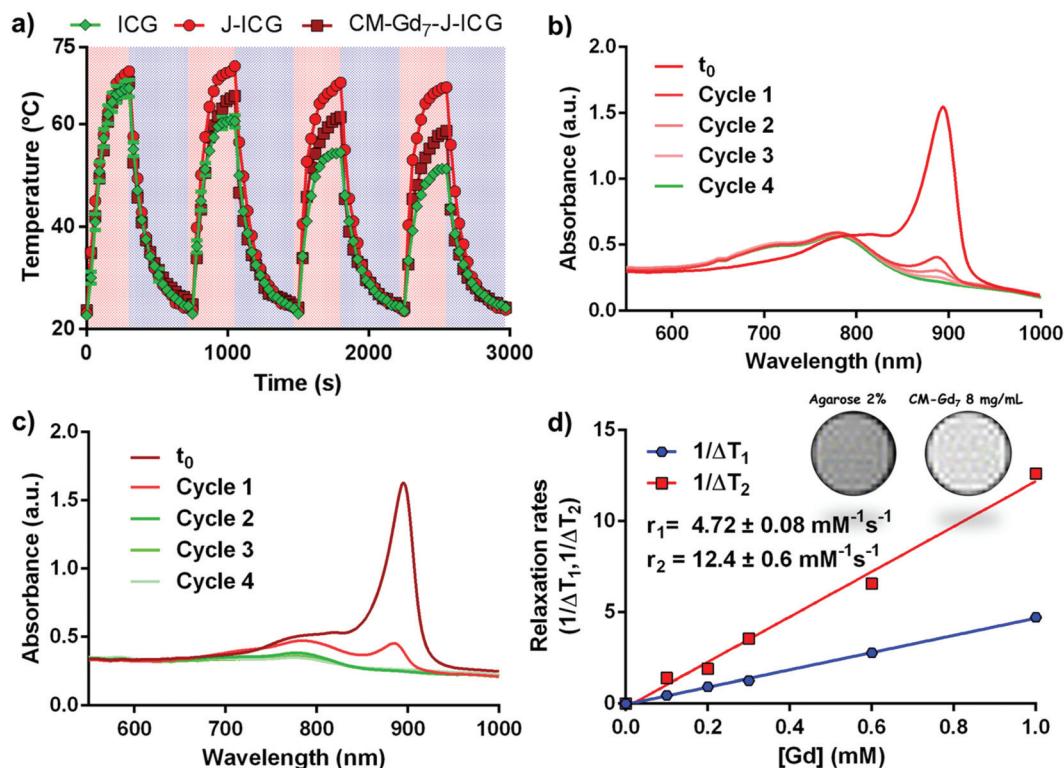

Fig. 4 (a) Temperature changes of ICG, J-ICG, and CM-Gd$_7$-J-ICG aqueous dispersion at the concentration of 25 μg mL^{-1} over four cycles of NIR-laser irradiation. Evolution of UV spectra of (b) J-ICG and (c) CM-Gd$_7$-J-ICG after each cycle of NIR-laser irradiation. (d) T_1 and T_2 relaxivities (r_1, r_2) for CM-Gd$_7$ nanocarrier. Inset: T_1-Weighted MR images of 2 wt% agarose and 8 mg mL^{-1} CM-Gd$_7$.

erty combined with the NIRFI ability of the cyanine dye turn this nanoplatform into an attractive alternative for smart nanotheranostic. To confirm CM-Gd$_7$-J-ICG capabilities as an MRI contrast agent, we measured the T_1 and T_2 relaxation time of the micelles at different concentrations. Relaxivities r_1 and r_2 were 4.72 and 12.40 mM^{-1} s^{-1}, respectively (Fig. 4d). Interestingly, CM-Gd$_7$ has an r_1 value comparable to other commercially available Gd-based contrast agents, such as Magnevist (4.25 mM^{-1} s^{-1}).[46] In this point, it is worth mentioning that the incorporation of J-ICG did not significantly affect the MRI ability of the protein nanocarrier as r_1 of CM-Gd$_7$-J-ICG was 4.02 mM^{-1} s^{-1}, suggesting a negligible Gd^{3+}/dye interaction (see Fig. S6†). These values make the system a promising T_1 contrast agent at standard doses.

In order to characterize the performance of CM-Gd$_7$-J-ICG nanoprobes in the biological system, we studied their *in vitro* cellular uptake by microscopy. For reference, we included free J-ICG and ICG in the uptake study at equivalent concentrations, as well as non-loaded micelles as a control. HeLa cells were incubated with the different agents for 6 h and then imaged in a confocal laser-scanning microscope using the same settings for all samples. As previously reported, ICG fluorescence is completely quenched when monomers self-assemble in J-aggregates (see Fig. S7†).[26] Nevertheless, strong fluorescence signals could be seen in the cytoplasm of HeLa cells incubated with CM-Gd$_7$-J-ICG (Fig. 5a), indicating that J-ICG could be partially dissociated into ICG monomer when micelles are efficiently internalized into cells. Although deeper
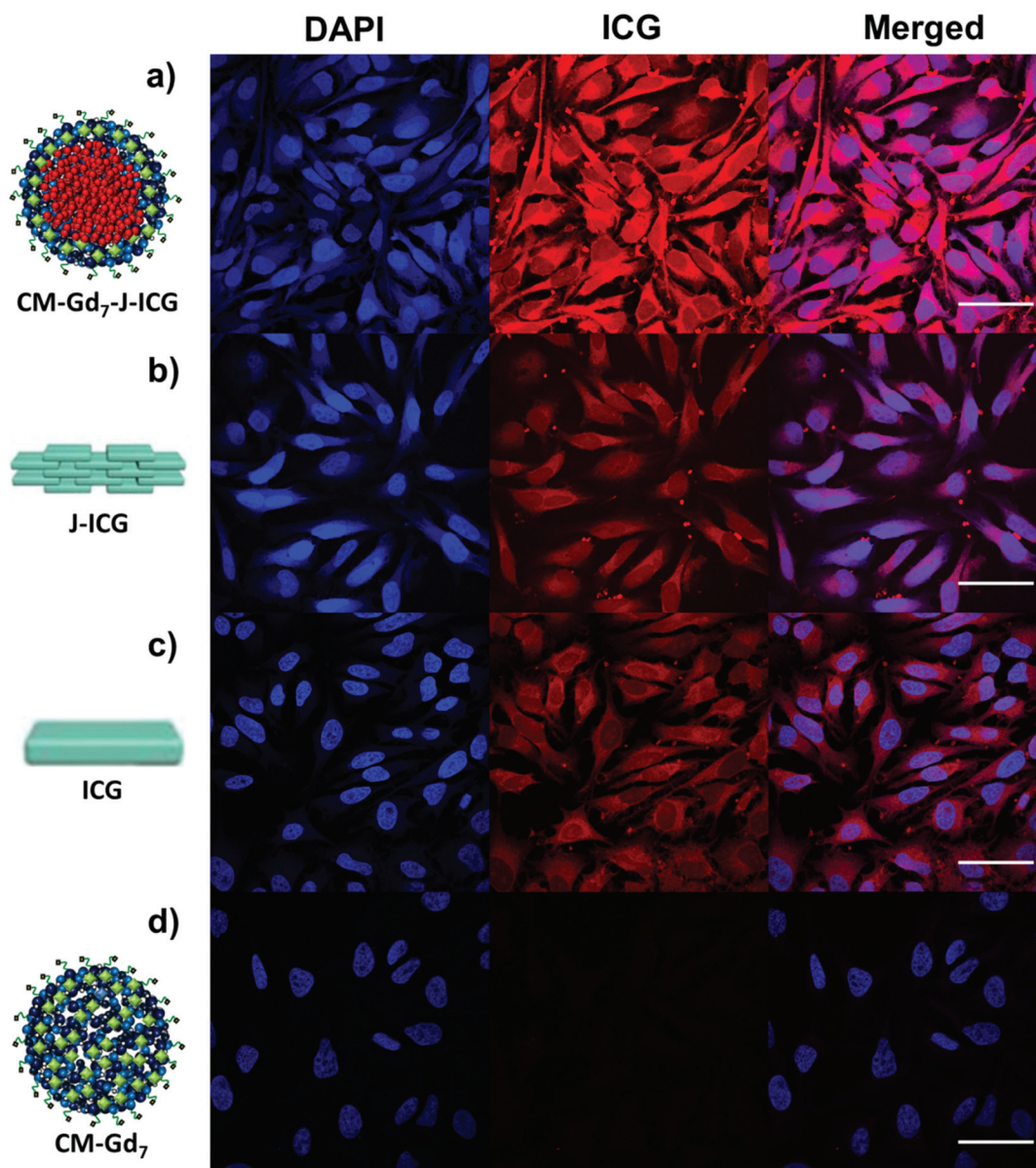

Fig. 5 Confocal laser scanning microscopy images of HeLa cells incubated for 6 h with (a) CM-Gd$_7$-J-ICG nanoprobe, (b) J-ICG, (c) ICG monomer, and (d) CM-Gd$_7$. Blue: nuclei stained with DAPI, red: ICG. Scale bar: 50 μm.
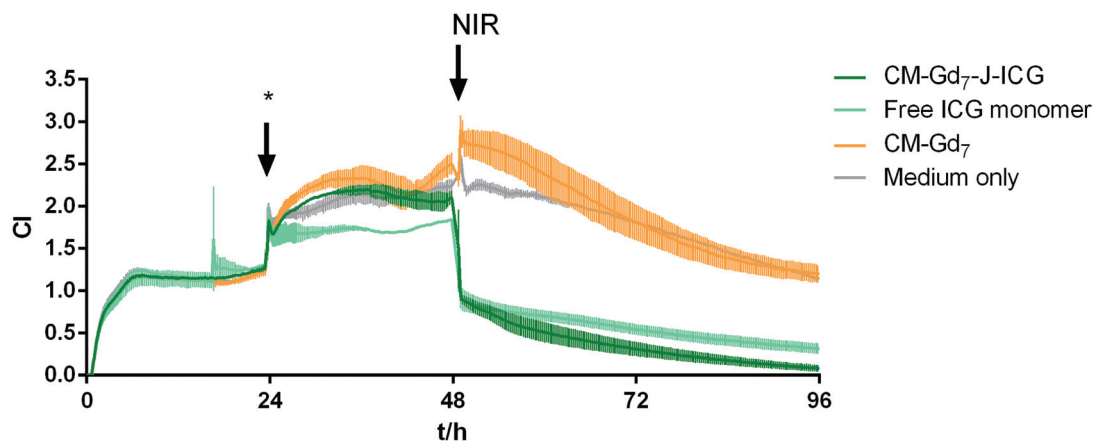
Fig. 6 Real-time cell analysis of HeLa cells incubated with CM-Gd$_7$-J-ICG, free ICG monomer, CM-Gd$_7$, and medium only. 24 h after seeding, the compounds were added (*) and after another 24 h, cells were irradiated with a NIR laser for 5 minutes.

biological studies are needed to shed light on this phenomenon, internalization-responsive fluorescence might result from intracellular dye leakage followed by strong interactions with amphiphilic membrane proteins and phospholipids.[26] Interestingly, CCM-Gd$_7$-J-ICG showed a higher fluorescence intensity inside the cells than free J-ICG (Fig. 5b) and ICG (Fig. 5c), which allows speculating that encapsulation of the dye increased its internalization. These results clearly show that CM-Gd$_7$-J-ICG hold great promise as a nanotheranostic combining MIR and NIRFI diagnostic modalities.

As a proof of concept for the application as theranostic PTT agents, we used real-time cell analysis (RTCA) to investigate the influence of CM-Gd$_7$-J-ICG on cell viability and morphology over time, and after irradiation with NIR light (Fig. 6). HeLa cells incubated with culture medium alone, free ICG and empty CM-Gd$_7$ micelles were used as a control.

We found that cells incubated with CM-Gd$_7$ and CM-Gd$_7$-J-ICG showed a very similar growth profile as cells treated with medium only, as can be seen by their similar cell indices (CI) over time. However, cells incubated with free ICG showed a stagnating cell growth, with the growth curve flattened. These results demonstrate the very good compatibility of the carrier with the cells, as expected, but also confirm that we can indeed reduce some negative side effects of free ICG by encapsulation of its assembled form into casein micelles.

After NIR irradiation, cells incubated with ICG and CCM-Gd$_7$-J-ICG were highly affected, as seen by a large drop in their cell index values. This observation can be attributed to the strong generation of heat by the photothermal agents, causing immediate cell death by ablation. Irradiation of cells treated with CM-Gd$_7$ alone and medium alone had however, no discernible effect (also compare to Fig. S8†). As free J-ICG is not stable in biological environments and rapidly dissociates into its monomeric form, it was excluded from this experiment. These results show the great potential of CCM-Gd$_7$-J-ICG as a therapeutic nanoagent and encourage us to extend this research to more complex microenvironments, as solid tumors

in future studies, where the benefits of the J-aggregates will be assessed in detail.

3. Conclusions

We have explored an innovative approach to tackle the photo-degradability of ICG, relying on the stabilization of J-type aggregates in hydrophobic protein pockets which can act as depots of the dye monomer/dimer forms through an equilibrium-driven mechanism. To validate this concept we fabricated a biodegradable casein-based nanocarrier using gadopentetic acid as a crosslinking agent. This complex provided the nanocarriers with high stability in physiological media and against dissociating agents, and generated sizes in the range between 140 and 165 nm. We found that by varying the crosslinking density of the protein micelles its degradation rate by cathepsin B, a tumor-associated protease, could be controlled beneficially to ensure body clearance after treatment. The design of this nanoagent was also aimed to address the poor stability of the J-ICG in biological environments, a major problem that limits their therapeutic outcome. By encapsulating this self-assembled dye into the micelles, its dissociation under dilute conditions was significantly slowed down or even hindered for at least 10 days. Therefore, it is expected that J-aggregates are stable in serum after parenteral administration expanding the prospects of these nano-assemblies for *in vivo* applications. Once stabilized within the micelles, J-ICG promotes the continuous supply of monomer/dimer allowing multiple irradiation cycles with superior photothermal performance as compared to free ICG. The main pitfall of the confinement of J-ICG was found to be an acceleration of their disassembly rate in comparison to free J-ICG. Although the reasons for this behavior are still under investigation, we hypothesized that J-ICG may be degraded at high temperatures in the confined environment. Nevertheless, we could confirm the excellent compatibility of the carriers with cultured cells *in vitro*:

while the free ICG had a negative effect on cell growth, incubation with the carrier alone as well as the carrier with encapsulated J-ICG left the cells unaffected. After irradiation with NIR light however, sufficient heat to cause immediate cell death by ablation was developed, confirming the functionality and potential as a photothermal agent.

In summary, this novel approach of equilibrium-driven monomer dye supply combined with our functional nanocarrier allowed to create an innovative nanoplatform that can simultaneously serve as an MRI/NIRFI multimodal probe and an effective photothermal agent for smart theranostics. The concept of J-aggregates confinement in polymer nanocarriers becoming a new paradigm for theranostic is still in its infancy, but it is foreseen that this work will lay the foundation for future investigations focusing on new strategies of stabilization for other cyanine dyes.

4. Experimental

4.1. Materials

The following chemicals were used as purchased: Casein sodium salt from bovine milk (Sigma-Aldrich); diethylenetriaminepentaacetic acid gadolinium(III) dihydrogen salt hydrate (DTPAGd, 97%, Sigma-Aldrich); N-(3-dimethylaminopropyl)-N'-ethylcarbodiimide hydrochloride (EDC, Sigma-Aldrich); N-hydroxysuccinimide (NHS, Sigma-Aldrich); indocyanine green (ICG, polymethine dye, Sigma-Aldrich), calcium chloride dihydrate ($CaCl_2 \cdot 2H_2O$, Grüssing), sodium chloride (NaCl, VWR Chemicals), acetic acid glacial (CH_3COOH, Fisher Chemicals), sodium acetate ($C_2H_3NaO_2$, Grüssing), sodium dihydrogen phosphate (NaH_2PO_4, Grüssing), disodium hydrogen phosphate (Na_2HPO_4, Grüssing), urea (ReagentPlus®, ≥99.5%, Sigma-Aldrich), microscopy grade uranyl acetate 1 wt% solution (UAc, EMS), deuterium oxide (D_2O, Sigma-Aldrich), cathepsin B from human placenta (≥5 units per mg protein, Sigma-Aldrich), ethylenediaminetetraacetic acid (EDTA, BioUltra, ≥99% Sigma-Aldrich), dithiothreitol (DTT, BioXtra ≥99%, Sigma-Aldrich) and 3-(4,5-dimethylthiazol-2-yl)-2,5-diphenyltetrazolium bromide (MTT, Sigma-Aldrich). Ultrapure water was used throughout the work.

4.2 Synthesis of Gd-decorated casein micelles

We firstly re-assembled casein micelles (CM) from sodium caseinate following a previously reported protocol.[34] Briefly, protein solution (50 mg mL^{-1}) was dialyzed against a 0.5 mM $CaCl_2$ solution for 4 h, using a dialysis membrane with a molecular weight cut off (MWCO) of 10 kDa. After the dialysis process, re-assembled micelles were kept at 4 °C for 24 h and then centrifuged at 10 000 rpm for 10 min to precipitate protein aggregates. Ultimately, re-constituted micelles were crosslinked with different amounts of DTPAGd (0.2–0.9 mg mL^{-1}) aiming to endow the nanocarriers with both colloidal stability and MRI ability. For this, the crosslinking agent was firstly activated with EDC and NHS (at a molar ratio of 1 : 2 : 2)

in phosphate-buffered saline (PBS, pH 6.9, 0.1 M) for 2 h. Then, the activated DTPAGd solution was added to micelles dispersion (at a final concentration of 10 mg mL^{-1}), previously heat up to 70 °C for 30 min, and it left reacting for 2 h. The obtained Gd-decorated crosslinking micelles were purified by dialysis (MWCO = 1000 kDa) for 48 h in water and subsequently stored at 4 °C. The products were named as CM-Gd$_2$, CM-Gd$_4$, CM-Gd$_6$, and CM-Gd$_7$ according to their functionalization values of 1.6, 4.4, 6.4, and 7.3% in weight of the Gd^{3+}-decorated CM.

4.3 Size and structural stability of the CM-Gd

The hydrodynamic diameter (Z-average) and polydispersity index (PDI) of the nanoprobes was measured by dynamic light scattering (DLS) using a Zetasizer Nano ZS (Malvern Instruments). Measurements were carried out at a scattering angle of 173° and a laser wavelength of 633 nm. Dispersions (1 mg mL^{-1}) in water, 10 mM PBS pH 7.4, or 10 mM acetate-buffered saline (ABS) pH 5, respectively, were measured at 25 and 37 °C. DLS was also used to study the structural and colloidal stability of the micelles against urea as a dissociating agent. Micelles dispersions (8 mg mL^{-1}) were diluted until 1 mg mL^{-1} in 8 M urea at pH 9.3. Non-crosslinked micelles (non-CM) were used as control.

Nanoparticle tracking analysis (NTA) was performed to further confirm the crosslinked nature of the nanocarriers. NTA measurements were carried out using a NanoSight NS500 equipment (Malvern) at 25 °C from water-diluted samples (2 × 10^{-4} mg mL^{-1}, much lower than the CAS critical micellar concentration, 0.1 mg mL^{-1}).

4.4 Determination of Gd concentration in CM-Gd

The concentration of Gd^{3+} in CM-Gd samples was measured by inductively coupled plasma mass spectrometry (ICP-MS). All samples were digested using microwave-assisted acid digestion with 69% HNO$_3$ and 30% H$_2$O$_2$ for 30 min at 200 °C and 160 bars. Measurements were performed with a quadrupole ICP mass spectrometer (iCAP-Q, Thermo Fisher Scientific GmbH, Dreieich, Germany) equipped with a PFA ST Nebulizer, a quartz cyclonic spray chamber, and a 2.5 mm quartz injector (all from Thermo Fisher Scientific) using the 158Gd and 103Rh as an internal standard. Calibrations were performed using an ionic standard of DTPAGd in 3.5% HNO$_3$ solutions ranging from 0.1 to 100 ppb. The internal standard was added to each sample. The gas flow for the cool gas and the auxiliary gas were set to 14 L min^{-1}, and 0.65 L min^{-1} respectively. The sample flow rate was 0.4 mL min^{-1}. All isotopes were analysed using the collision cell technique at 5 mL min^{-1} collision gas flow (93% He and 7% H$_2$).

4.5 Degradability of the CM-Gd against proteases

The proteolytic degradation of the nanosystems was analyzed by DLS following the change of their hydrodynamic diameters over time. Cathepsin B was used as model protease, as it is commonly overexpressed in several malignant tumors. Thus, 10 μL of 2 mM EDTA, 10 μL of 5 mM DTT, and 5 μL of cathep-

sin B (100 units per mL) were added to 75 µL of CM-Gd (8 mg mL^{-1}) and their size was immediately measured each 90 min, for 24 h at 37.0 ± 0.5 °C.

4.6 Scanning transmission electron microscopy (STEM)

The morphology of Gd-decorated micelles was studied by means of STEM using a Hitachi SU8030 microscope. To this effect, a drop of diluted dispersion (0.01 wt% of solids content) was placed on a carbon-coated copper grid. After drying, a drop of 1 wt% UAc solution was added as a staining agent.

4.7 Preparation of ICG J-aggregates

J-ICG were prepared following the procedure described elsewhere.[44] Briefly, ICG aqueous solution (10 mg mL^{-1}) was heated at 65 °C for 20 h and then dialyzed against water for 24 h to remove any free dye. The formation of J-ICG was confirmed by UV-Vis spectroscopy using a Cary 100 Bio equipment (Agilent). Finally, the J-aggregates solution was stored at 4 °C for later utilization.

4.8 Loading of J-ICG into CM-Gd nanoprobes

For J-ICG loading, different amounts of dye nanoaggregates (1–15% based on protein) were added to the micelle dispersion (8 mg mL^{-1}) and magnetically stirred overnight. The CM-Gd-J-ICG nanoprobe was purified using a Vivaspin™ tube (MWCO 1000 kDa) centrifuging at 6000 rpm for 10 min and washing with water. Several cycles were performed until free J-aggregates were not detected in the washing water by UV–Vis spectroscopy.

The *in situ* formation of J-ICG within CM-Gd was evaluated through the encapsulation of ICG monomer into the protein nanoprobe, followed by either heating of the micelle dispersion at 65 °C for 20 h or aging at 4 °C for 7 days. For ICG loading and nanocarrier purification, the same procedure as for J-ICG was used.

The encapsulated amounts of J-ICG or ICG were calculated by UV–Vis spectroscopy, measuring the absorbance of the dyes at 895 or 780 nm, respectively, and correlated with a calibration curve in water (see Fig. S9 of the ESI†). Encapsulation efficiency (EE) was defined as the weight percentage of the dye loaded *versus* the amount added to the micelles dispersion and loading capacity (LC) was calculated as the weight percentage of dye relative to the micelles.

The stability of J-ICG into CM-Gd was evaluated following the evolution over time of the characteristic J-ICG trace in the UV-Vis region using non-encapsulated J-ICG as a control. The measurements were carried out at a dye concentration of 5 µg mL^{-1}.

4.9 *In vitro* laser irradiation of the photothermal nanoagents

The heat production of ICG, J-ICG, and CM-Gd$_7$-J-ICG nanoprobes was measured at 25 µg mL^{-1}, placing a 100 µL sample in a transparent Eppendorf tube and irradiating with an infrared diode laser module (FC-D-785 CNI, λ = 785 nm, 500 mW). The solution was irradiated for 300 s (ON) and then cooled for 420 s (OFF). During ON/OFF cycle, the temperature variation was monitored with an infrared camera (FLIR E30, 25° Optic, 60 Hz). The ON/OFF cycle was repeated four times, and samples were tested in triplicate. Additionally, the photothermal stability of the theranostic nanoagents after each ON/OFF cycle was evaluated by UV–Vis spectroscopy at 5 µg mL^{-1} dye concentration. The photothermal conversion efficiency (η) of J-ICG and CM-Gd-J-ICG was determined from the steady-state temperature rise of 5 µg mL^{-1} dispersions, using the following equation according to Korgel *et al.*[47] (see ESI† for calculation details):

$$\eta = \frac{hA(T_{\max} - T_{\text{surr}}) - Q_{\text{in,surr}}}{I(1 - 10^{-A_\lambda})} \tag{1}$$

where h is the heat transfer coefficient, A is the surface area of the container, $T_{\max}$ is the maximum steady-state temperature, T_{surr} is the ambient surrounding temperature, I is the laser power, A_λ is the absorbance at the excitation wavelength of 785 nm. $Q_{\text{in,surr}}$ is the heat input due to light absorption by the solvent, which was measured independently and found to be 3.25 mW. The quantity hA was calculated by measuring the rate of temperature drop after removing the laser source (see ESI† for calculation details).

4.10 MRI ability of the CM-Gd nanoprobe

CM-Gd$_7$ dispersions with different Gd^{3+} concentrations ranging from 0.1 mM to 1 mM were prepared in a 2 wt% agarose gel and scanned at 25 °C on a Magritek Kea2 spectrometer operating at 60 MHz for ^{1}H. A 1.4 T permanent magnet (Varian EM360) was used. Inversion recovery and spin-echo pulse sequences were used for T_1 and T_2 measurements, respectively. Relaxivities, r_1 and r_2 were calculated by plotting the relaxation rates ($1/\Delta T_1$ and $1/\Delta T_2$) for each sample against the Gd^{3+} concentration.

4.11. Cellular uptake

Cellular uptake was visualized by confocal laser scanning microscopy. For this, HeLa cells were seeded onto coverslips in 24 well plates at a density of 10 000 cells per mL in full culture medium and incubated overnight at 37 °C and 5% CO$_2$. The next day, compounds were added and incubated for 6 h at 37 °C. Then, the cell culture supernatant was removed, cells were washed 3× with PBS and fixed for 20 minutes with 10% neutral buffered formalin at room temperature. After 3× washing with PBS, nuclei were stained with DAPI (Carl Roth, 2.5 µg mL^{-1} in PBS) for 30 minutes and washed again before mounting on microscope slides using ProTaqs(R) MountFluor mounting medium (Quartett GmbH). Images were acquired using LASX software on a Leica SP8 system. Fluorescence was collected in red channel: Ex 633 nm, Em 700–800 nm.

4.12 *In vitro* monitoring of cells treated with nanoagents and NIR irradiation

We monitored the influence of the nanoagents on cells with and without NIR irradiation using real-time cell analysis

(RTCA) on an xCELLigence DP system (ACEA Biosciences Inc.). 10 000 HeLa cells per well were seeded into two E-plates 16 and grown for 24 h. Then, fresh medium including either CM-Gd$_7$, free ICG monomer, free J-ICG, and CM-Gd$_7$-J-ICG was added. Two plates were prepared identically. After another 24 h, E-plates were released from the device and respective wells of one E-plate were irradiated for 5 minutes with a NIR laser (FC-D-785 CNI, λ = 785 nm, 500 mW) from a distance of 2 cm. The other E-plate was treated the same (handling control) but not irradiated (see Fig. S8†). Cell indices (CI) are derived from impedance measurements through gold electrodes on the bottom of the E-plate wells, where the impedance corresponds to the surface area covered by cells. The area covered by cells is influenced by their morphology (spread out *vs.* rounded up) and number of cells, which allows drawing conclusions about the cell proliferation and death events. Monitoring was continued for another 2 days after irradiation.

Conflicts of interest

There are no conflicts to declare.

Acknowledgements

References

1 H. Zhu, P. Cheng, P. Chen and K. Pu, Recent Progress in the Development of Near-Infrared Organic Photothermal and Photodynamic Nanotherapeutics, *Biomater. Sci.*, 2018, **6**(4), 746–765, DOI: 10.1039/c7bm01210a.

2 B. Liu, C. Li, Z. Cheng, Z. Hou, S. Huang and J. Lin, Functional Nanomaterials for Near-Infrared-Triggered Cancer Therapy, *Biomater. Sci.*, 2016, 890–909, DOI: 10.1039/c6bm00076b.

3 J. Wang, X. Wang, S. Y. Lu, J. Hu, W. Zhang, L. Xu, D. Gu, W. Yang, W. Tang, F. Liu, Y. Cao and H. Liu, Integration of Cascade Delivery and Tumor Hypoxia Modulating Capacities in Core-Releasable Satellite Nanovehicles to Enhance Tumor Chemotherapy, *Biomaterials*, 2019, **223**, 119465, DOI: 10.1016/j.biomaterials.2019.119465.

4 R. Liang, Y. Li, M. Huo, H. Lin and Y. Chen, Triggering Sequential Catalytic Fenton Reaction on 2D MXenes for Hyperthermia-Augmented Synergistic Nanocatalytic Cancer Therapy, *ACS Appl. Mater. Interfaces*, 2019, **11**(46), 42917–42931, DOI: 10.1021/acsami.9b13598.

5 G. Gao, Y. W. Jiang, Y. Guo, H. R. Jia, X. Cheng, Y. Deng, X. W. Yu, Y. X. Zhu, H. Y. Guo, W. Sun, X. Liu, J. Zhao, S. Yang, Z. W. Yu, F. M. S. Raya, G. Liang and F. G. Wu, Enzyme-Mediated Tumor Starvation and Phototherapy Enhance Mild-Temperature Photothermal Therapy, *Adv. Funct. Mater.*, 2020, **30**(16), 1909391, DOI: 10.1002/adfm.201909391.

6 J. Cao, B. Qiao, Y. Luo, C. Cheng, A. Yang, M. Wang, X. Yuan, K. Fan, M. Li and Z. Wang, A Multimodal Imaging-Guided Nanoreactor for Cooperative Combination of Tumor Starvation and Multiple Mechanism-Enhanced Mild Temperature Phototherapy, *Biomater. Sci.*, 2020, **8**(23), 6561–6578, DOI: 10.1039/d0bm01350a.

7 M. Molina, S. Wedepohl and M. Calderón, Polymeric Near-Infrared Absorbing Dendritic Nanogels for Efficient in Vivo Photothermal Cancer Therapy, *Nanoscale*, 2016, **8**(11), 5852–5856, DOI: 10.1039/c5nr07587d.

8 R. Chen, X. Zheng, H. Qian, X. Wang, J. Wang and X. Jiang, Combined Near-IR Photothermal Therapy and Chemotherapy Using Gold-Nanorod/Chitosan Hybrid Nanospheres to Enhance the Antitumor Effect, *Biomater. Sci.*, 2013, **1**(3), 285–293, DOI: 10.1039/c2bm00138a.

9 Y. Hernández and B. C. Galarreta, Noble Metal-Based Plasmonic Nanoparticles for SERS Imaging and Photothermal Therapy, in *Nanomaterials for Magnetic and Optical Hyperthermia Applications*, 2018, pp 83–109. DOI: 10.1016/B978-0-12-813928-8.00004-1.

10 J. T. Robinson, S. M. Tabakman, Y. Liang, H. Wang, H. Sanchez Casalongue, D. Vinh and H. Dai, Ultrasmall Reduced Graphene Oxide with High Near-Infrared Absorbance for Photothermal Therapy, *J. Am. Chem. Soc.*, 2011, **133**(17), 6825–6831, DOI: 10.1021/ja2010175.

11 Z. M. Markovic, L. M. Harhaji-Trajkovic, B. M. Todorovic-Markovic, D. P. Kepić, K. M. Arsikin, S. P. Jovanović, A. C. Pantovic, M. D. Dramićanin and V. S. Trajkovic, In Vitro Comparison of the Photothermal Anticancer Activity of Graphene Nanoparticles and Carbon Nanotubes, *Biomaterials*, 2011, **32**(4), 1121–1129, DOI: 10.1016/j.biomaterials.2010.10.030.

12 Z. Chen, Z. Li, J. Wang, E. Ju, L. Zhou, J. Ren and X. Qu, A Multi-Synergistic Platform for Sequential Irradiation-Activated High-Performance Apoptotic Cancer Therapy, *Adv. Funct. Mater.*, 2014, **24**(4), 522–529, DOI: 10.1002/adfm.201301951.

13 Q. Chen, C. Wang, Z. Zhan, W. He, Z. Cheng, Y. Li and Z. Liu, Near-Infrared Dye Bound Albumin with Separated Imaging and Therapy Wavelength Channels for Imaging-Guided Photothermal Therapy, *Biomaterials*, 2014, **35**(28), 8206–8214, DOI: 10.1016/j.biomaterials.2014.06.013.

14 A. Puiggalí-Jou, S. Wedepohl, L. E. Theune, C. Alemán and M. Calderón, Effect of Conducting/Thermoresponsive Polymer Ratio on Multitasking Nanogels, *Mater. Sci. Eng., C*, 2021, **119**, 111598, DOI: 10.1016/j.msec.2020.111598.

15 S. Wang, J. Lin and P. Huang, Advances on the Use of Biodegradable Proteins/Peptides in Photothermal Theranostics, *J. Nanomater.*, 2016, **2016**, 5810952, DOI: 10.1155/2016/5810952.

16 H. S. Jung, P. Verwilst, A. Sharma, J. Shin, J. L. Sessler and J. S. Kim, Organic Molecule-Based Photothermal Agents: An Expanding Photothermal Therapy Universe, *Chem. Soc. Rev.*, 2018, 2280–2297, DOI: 10.1039/c7cs00522a.

17 H. Wang, X. Li, B. W. C. Tse, H. Yang, C. A. Thorling, Y. Liu, M. Touraud, J. B. Chouane, X. Liu, M. S. Roberts and X. Liang, Indocyanine Green-Incorporing Nanoparticles for Cancer Theranostics, *Theranostics*, 2018, 1227–1242, DOI: 10.7150/thno.22872.

18 H. J. Yoon, H. S. Lee, J. Y. Lim and J. H. Park, Liposomal Indocyanine Green for Enhanced Photothermal Therapy, *ACS Appl. Mater. Interfaces*, 2017, **9**(7), 5683–5691, DOI: 10.1021/acsami.6b16801.

19 L. Wu, S. Fang, S. Shi, J. Deng, B. Liu and L. Cai, Hybrid Polypeptide Micelles Loading Indocyanine Green for Tumor Imaging and Photothermal Effect Study, *Biomacromolecules*, 2013, **14**(9), 3027–3033, DOI: 10.1021/bm400839b.

20 L. Yu, A. Dong, R. Guo, M. Yang, L. Deng and J. Zhang, DOX/ICG Coencapsulated Liposome-Coated Thermosensitive Nanogels for NIR-Triggered Simultaneous Drug Release and Photothermal Effect, *ACS Biomater. Sci. Eng.*, 2018, **4**(7), 2424–2434, DOI: 10.1021/acsbiomaterials.8b00379.

21 Z. Sheng, D. Hu, M. Xue, M. He, P. Gong and L. Cai, Indocyanine Green Nanoparticles for Theranostic Applications, *Nano-Micro Lett.*, 2013, 145–150, DOI: 10.5101/nml.v5i3.p145-150.

22 M. Sevieri, F. Silva, A. Bonizzi, L. Sitia, M. Truffi, S. Mazzucchelli and F. Corsi, Indocyanine Green Nanoparticles: Are They Compelling for Cancer Treatment?, *Front. Chem.*, 2020, **8**, 535, DOI: 10.3389/fchem.2020.00535.

23 E. E. Jelley, Spectral Absorption and Fluorescence of Dyes in the Molecular State, *Nature*, 1936, **138**(3502), 1009–1010, DOI: 10.1038/1381009a0.

24 G. Scheibe, Über die Veränderlichkeit der Absorptionsspektren in Lösungen und die Nebenvalenzen als ihre Ursache, *Angew. Chem., Int. Ed.*, 1937, **50**, 212, DOI: 10.1002/ange.19370501103.

25 A. Eisfeld and J. S. Briggs, The J- and H-Bands, of Organic Dye Aggregates, *Chem. Phys.*, 2006, **324**(2), 376–384, DOI: 10.1016/j.chemphys.2005.11.015.

26 R. Liu, J. Tang, Y. Xu, Y. Zhou and Z. Dai, Nano-Sized Indocyanine Green J-Aggregate as a One-Component Theranostic Agent, *Nanotheranostics*, 2017, **1**(4), 430–439, DOI: 10.7150/ntno.19935.

27 A. K. Kirchherr, A. Briel and K. Mäder, Stabilization of Indocyanine Green by Encapsulation within Micellar Systems, *Mol. Pharm.*, 2009, **6**(2), 480–491, DOI: 10.1021/mp8001649.

28 B. Changalvaie, S. Han, E. Moaseri, F. Scaletti, L. Truong, R. Caplan, A. Cao, R. Bouchard, T. M. Truskett, K. V. Sokolov and K. P. Johnston, Indocyanine Green J Aggregates in Polymersomes for Near-Infrared Photoacoustic Imaging, *ACS Appl. Mater. Interfaces*, 2019, **11**(50), 46437–46450, DOI: 10.1021/acsami.9b14519.

29 Z. Sheng, D. Hu, M. Zheng, P. Zhao, H. Liu, D. Gao, P. Gong, G. Gao, P. Zhang, Y. Ma and L. Cai, Smart Human Serum Albumin-Indocyanine Green Nanoparticles Generated by Programmed Assembly for Dual-Modal Imaging-Guided Cancer Synergistic Phototherapy, *ACS Nano*, 2014, **8**(12), 12310–12322, DOI: 10.1021/nn5062386.

30 F. An, Z. Yang, M. Zheng, T. Mei, G. Deng, P. Guo, Y. Li and R. Sheng, Rationally Assembled Albumin/Indocyanine Green Nanocomplex for Enhanced Tumor Imaging to Guide Photothermal Therapy, *J. Nanobiotechnol.*, 2020, **18**(1), 49, DOI: 10.1186/s12951-020-00603-8.

31 L. Sitia, M. Sevieri, A. Bonizzi, R. Allevi, C. Morasso, D. Foschi, F. Corsi, F. Corsi, F. Corsi and S. Mazzucchelli, Development of Tumor-Targeted Indocyanine Green-Loaded Ferritin Nanoparticles for Intraoperative Detection of Cancers, *ACS Omega*, 2020, **5**(21), 12035–12045, DOI: 10.1021/acsomega.0c00244.

32 J. C. Cuggino, F. E. Ambrosioni, M. L. Picchio, M. Nicola, Á. F Jiménez Kairuz, G. Gatti, R. J. Minari, M. Calderón, C. I. Alvarez Igarzabal and L. M. Gugliotta, Thermally Self-Assembled Biodegradable Poly(Casein-g-N-Isopropylacrylamide) Unimers and Their Application in Drug Delivery for Cancer Therapy, *Int. J. Biol. Macromol.*, 2020, **154**, 446–455, DOI: 10.1016/j.ijbiomac.2020.03.138.

33 S. Kaur, C. Prasad, B. Balakrishnan and R. Banerjee, Trigger Responsive Polymeric Nanocarriers for Cancer Therapy, *Biomater. Sci.*, 2015, **3**(7), 955–987, DOI: 10.1039/c5bm00002e.

34 M. L. Picchio, J. C. Cuggino, G. Nagel, S. Wedepohl, R. J. Minari, C. I. Alvarez Igarzabal, L. M. Gugliotta and M. Calderón, Crosslinked Casein-Based Micelles as a Dually Responsive Drug Delivery System, *Polym. Chem.*, 2018, **9**(25), 3499–3510, DOI: 10.1039/c8py00600h.

35 Q. Chen, C. Liang, X. Wang, J. He, Y. Li and Z. Liu, An Albumin-Based Theranostic Nano-Agent for Dual-Modal Imaging Guided Photothermal Therapy to Inhibit Lymphatic Metastasis of Cancer Post Surgery, *Biomaterials*, 2014, **35**(34), 9355–9362, DOI: 10.1016/j.biomaterials.2014.07.062.

36 X. Liang, Y. Li, X. Li, L. Jing, Z. Deng, X. Yue, C. Li and Z. Dai, PEGylated Polypyrrole Nanoparticles Conjugating Gadolinium Chelates for Dual-Modal MRI/Photoacoustic Imaging Guided Photothermal Therapy of Cancer, *Adv. Funct. Mater.*, 2015, **25**(9), 1451–1462, DOI: 10.1002/adfm.201402338.

37 Y. Liu, Z. Chen, C. Liu, D. Yu, Z. Lu and N. Zhang, Gadolinium-Loaded Polymeric Nanoparticles Modified with Anti-VEGF as Multifunctional MRI Contrast Agents for the Diagnosis of Liver Cancer, *Biomaterials*, 2011, **32**(22), 5167–5176, DOI: 10.1016/j.biomaterials.2011.03.077.

38 J. Ma, H. Dong, H. Zhu, C. Li, Y. Li and D. Shi, Deposition of Gadolinium onto the Shell Structure of Micelles for

Integrated Magnetic Resonance Imaging and Robust Drug Delivery Systems, *J. Mater. Chem. B*, 2016, **4**(36), 6094–6102, DOI: 10.1039/C6TB01013J.

39 M. Grogna, R. Cloots, A. Luxen, C. Jérôme, C. Passirani, N. Lautram, J.-F. Desreux and C. Detrembleur, Polymer Micelles Decorated by Gadolinium Complexes as MRI Blood Contrast Agents: Design, Synthesis and Properties, *Polym. Chem.*, 2010, **1**(9), 1485–1490, DOI: 10.1039/C0PY00117A.

40 T. Hao, Q. Chen, Y. Qi, P. Sun, D. Chen, W. Jiang, K. Liu, H. Sun, L. Li, J. Ding and Z. Li, Biomineralized Gd2O3@HSA Nanoparticles as a Versatile Platform for Dual-Modal Imaging and Chemo-Phototherapy-Synergized Tumor Ablation, *Adv. Healthcare Mater.*, 2019, **8**(24), 1901005, DOI: 10.1002/adhm.201901005.

41 B. Vaia, M. A. Smiddy, A. L. Kelly and T. Huppertz, Solvent-Mediated Disruption of Bovine Casein Micelles at Alkaline PH, *J. Agric. Food Chem.*, 2006, **54**(21), 8288–8293, DOI: 10.1021/jf061417c.

42 T. Huppertz, M. a. Smiddy and C. G. de Kruif, Biocompatible Micro-Gel Particles from Cross-Linked Casein Micelles, *Biomacromolecules*, 2007, **8**, 1300–1305, DOI: 10.1021/bm061070m.

43 R. de la Rica, D. Aili and M. M. Stevens, Enzyme-Responsive Nanoparticles for Drug Release and Diagnostics, *Adv. Drug Delivery Rev.*, 2012, **64**(11), 967–978, DOI: 10.1016/j.addr.2012.01.002.

44 F. Rotermund, R. Weigand and A. Penzkofer, J-Aggregation and Disaggregation of Indocyanine Green in Water, *Chem. Phys.*, 1997, **20**(3), 385–392, DOI: 10.1016/S0301-0104(97)00151-1.

45 L. E. Theune, R. Charbaji, M. Kar, S. Wedepohl, S. Hedtrich and M. Calderón, Critical Parameters for the Controlled Synthesis of Nanogels Suitable for Temperature-Triggered Protein Delivery, *Mater. Sci. Eng., C*, 2019, **100**, 141–151, DOI: 10.1016/j.msec.2019.02.089.

46 B. Mehravi, M. Ahmadi, M. Amanlou, A. Mostaar, M. S. Ardestani and N. Ghalandarlaki, Conjugation of Glucosamine with Gd3+-Based Nanoporous Silica Using a Heterobifunctional ANB-NOS Crosslinker for Imaging of Cancer Cells, *Int. J. Nanomed.*, 2013, **8**(1), 3383–3394, DOI: 10.2147/IJN.S44829.

47 C. M. Hessel, V. P. Pattani, M. Rasch, M. G. Panthani, B. Koo, J. W. Tunnell and B. A. Korgel, Copper Selenide Nanocrystals for Photothermal Therapy, *Nano Lett.*, 2011, **11**(6), 2560–2566, DOI: 10.1021/nl201400z.